International Communications in Heat and Mass Transfer 146 (2023) 106877

Contents lists available at ScienceDirect

International Communications in Heat and Mass Transfer

journal homepage: www.elsevier.com/locate/ichmt

Numerical simulations of temperature inside the heart tissues to evaluate the performances of cryoablative probe

M. Potenza [a], C. Pisano [b], P. Coppa [a], G. Bovesecchi [c,*], S. Corasaniti [a], F. Barbero [a]

[a] Department of Industrial Engineering, University of Rome "Tor Vergata", Rome, Italy
[b] Department of Surgical Sciences, University of Rome "Tor Vergata", Rome, Italy
[c] Department of Enterprise Engineering, University of Rome "Tor Vergata", Rome, Italy

ARTICLE INFO

Keywords:
Cryo-ablation
Cryoballoon
Heat transfer
Ice front
Finite differences
Atrial fibrillation

ABSTRACT

In the present paper the behaviour of human cardiac tissue during cryo-ablation is simulated with a finite difference algorithm which solves the Pennes' equation including the phase change during freezing of the cardiac tissues. The evolution of temperatures at different points is calculated and the movement of the ice front is obtained from simulation results. All phenomena related to heat transfer in living tissue are considered: heat conduction, heat release and absorption due to heat capacity, metabolism and blood perfusion. Although the geometry and the assumed boundary conditions are quite simple, the structure of the developed model can be easily adapted to more complex geometries. Model results show for instance that with a power of 10 W tissues distant 0.5 mm from the probe are ablated, while the other tissues more than 0.5 mm remain at −20 °C, so undamaged The results also show that the outcome of cryo-ablation treatment depends on many parameters: operational parameters such as the power heat absorbed by the probe (i.e. the mass flow rate of the cryo-fluid) and the duration of therapy application; biothermal parameters such as metabolic heat flux and blood perfusion; thermophysical properties of the tissue. Among these the effects of both blood perfusion and metabolic rate result less influencing. The numerical model presented could be useful to estimate the best conditions for the application of the probe during treatment and the possible change of the cure parameters to adapt the therapy to different patients.

1. Introduction

Catheter ablation is a well- established treatment option for patients with symptomatic atrial fibrillation (*AF*), and pulmonary vein (*PV*) isolation is the treatment of choice for patients with paroxysmal and persistent drug-refractory *AF* [1]. While radiofrequency (*RF*) based *PV* isolation in combination with a 3D mapping system has long been considered the "gold standard", the cryo-balloon (*CB*) has become the most used alternative ablation tool for *PV* isolation. This technique involves inserting a cryoprobe into the pulmonary vein, which penetrates to the left atrium of the heart, and injecting nitrous oxide (N_2O, laughing gas) through appropriate nozzles. A part of the high pressure gas liquefies due to its isenthalpic expansion (Joule Thomson or Joule Kelvin expansion) when it passes through the nozzles, and reaches its saturation temperature (−88.48 °C). The mixture of liquid and vapour reaches the balloon surface, whose temperatures assume values between −80 and − 50 °C. When the probe touches the junction of the pulmonary vein with the heart wall, the cells responsible for atrial fibrillation located in this area are frozen and thus killed [1–4]. [5] accurately describes the procedure and tricks to be adopted to maximize the therapy effects and minimize the drawbacks. The procedure has a reputation for causing fewer complications than radiofrequency ablation [6] because the target cells are damaged in a more concentrated way. Indeed, regardless of the energy source, the lesions produced by hyperthermia are inevitably associated with some tissue destruction, increasing the risk of perforation and thromboembolic stroke. In contrast, tissue destruction by freezing results minimal and preserves the basic architecture of the tissue. The resulting lesions retain good tensile strength and are minimally thrombogenic.

Nevertheless, cryoballoon ablation is delicate and not risk free. The tip of the cryoprobe is close to the phrenic nerve [7], whose injury can lead to paralysis or death [8]. In addition, severe narrowing of the pulmonary veins has been observed in some cases as a result of the procedure.

It seems that a strict control of the trend of the ice front movement in

* Corresponding author.
E-mail address: gianluigi.bovesecchi@uniroma2.it (G. Bovesecchi).

https://doi.org/10.1016/j.icheatmasstransfer.2023.106877

Nomenclature

Latin

c	volumetric heat capacity [J·m^{-3}·K^{-1}]
d	distance [m]
Δt	time step [s]
k	thermal conductivity [W·m^{-1}·K^{-1}]
n	unit normal displacement to the ice front
q	volumetric heat generation [J·m^{-3}]
$\dot{q}$	volumetric heat generation per unit time [W·m^{-3}]
P	power [W]
r	generic radius [m]
R	radius [m]
t	time [s]
T	temperature [°C or K]
v	velocity [m·s^{-1}]
V	volume [m^3]

Greek

θ	smoothing function
ω	perfusion [s^{-1}]

Subscripts

a	artery
b	blood
f	frozen
l	latent
low	bottom
m	freezing/melting
met	metabolic
n	normal direction
u	unfrozen
up	top

Abbreviations

AF	Atrial Fibrillation
CB	CryoBalloon
FD	Finite Differences
PV	Pulmonary Vein
RF	Radio Frequency

human tissues is a fundamental task to achieve the desired safety and control of the surgical procedure. In this sense, experiments have already been performed with biological and synthetic samples [9], but not with the geometry or materials of the actual device, nor without the hardly reproducible blood perfusion [10]. Predicting and modelling the various degrees of damage to biological tissue caused by freezing is a complex issue [11], and correct numerical modelling based on experimental data is considered extremely useful for the functional settings of the cryogenic devices of the future [12].

Today, cryoablation of atrial fibrillation is performed worldwide. The most common probes are manufactured by Medtronic (2nd generation of the "Arctic Front Advance" probe [1,3,13]) and by Boston Scientific with the "PolarxTM" device [14]; a comparison of the two devices is described in [15] The Medtronic device is shown in Fig. 1. Cryoballoon ablation is usually performed under general anaesthesia. Under transoesophageal echocardiographic guidance, an 8.5-Fr. transeptal cannula with a Brockenbrough needle is advanced into the left atrium and exchanged for a steerable cryoballoon cannula. The cryoballoon is advanced into each *PV* ostium to obtain baseline electrical data. The cryoballoon is inflated and carefully advanced to seal each *PV*. Finally, the cryoenergy application is performed.

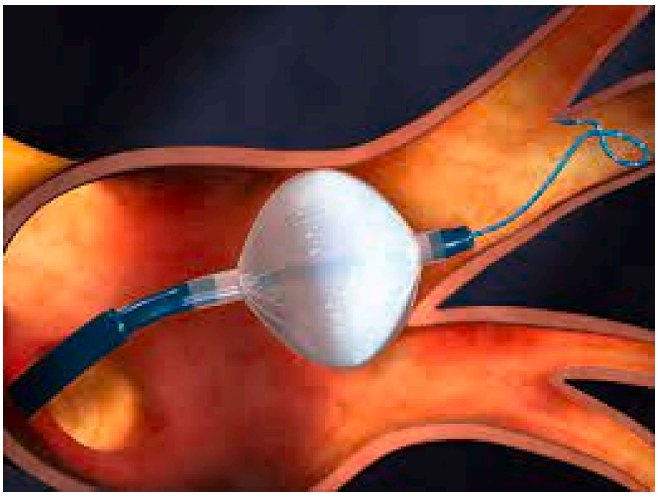

Fig. 1. Medtronic cryo-probe touching the pulmonary vein (courtesy by Medtronic) [1,3].

Application of the cryoprobe to a tissue surface results in the formation of a well-defined hemispherical block of frozen tissue called ice ball, which may have either oblate or prolate geometry. The cells within the ice ball are irreversibly damaged and eventually replaced by fibrotic tissue. In vivo and in vitro studies have shown that cardiac tissue is sensitive to freezing injury [16]. In their study, Weimar et al. set −20 °C as the lethal limit for myocardial cells in their study [17]. A lethal temperature range between −10 °C and − 25 °C was also confirmed when applied along a longer period of time [18]. Other ablation parameters have also been studied, such as cooling rate, tissue temperature, duration of freezing, thawing rate, repetition of the freeze-thaw cycle and interval between freeze-thaw cycles [19–21]. The reason to don't go under −25 °C is the need to preserve healthy tissues (as pulmonary veins and bronchus) surrounding the cryo-ablated zone, due to a more extended freezing propagation when lower temperatures are reached [22], or to avoid atrioesophageal fistulas [12].

According to different references [5, 12, 15, 16, 23], cryoablation is carried out applying different temperatures to the pulmonary veins, in the range − 50÷ − 20 °C, different TTI (time to isolation, when electric isolation is obtained in the charge carrying cells) in the range 60÷240 s, different number of chilly applications, from 1 to 4÷5. The practice of the cardiac surgery department of the University of Rome "Tor Vergata", headquarter of one of the authors, suggests only one application, TTI no shorter than 55÷60 s and temperatures of tissues to be ablated in the range − 20÷ − 25 °C. Balloon temperatures below −25 °C can easily produce damages to tissues in the neighbourhood, which must be preserved (e.g. the phrenic nerve).

To improve the results and performance of the procedure, the authors consider it necessary to study the physics and technology of the cryo-ablative process. It is possible to obtain information on the temperatures and heat flows involved through effective experimental tests, but these are difficult, expensive and require many replicates and equipment designs to obtain the desired parameter evaluation, which consequently costs a lot of time and money. The opportunity and usefulness of a numerical study comes from the possibility of freely varying the basic parameters of the system, i.e. temperatures, times, material properties and activities, with relatively little time and cost. Other authors have also studied how to achieve freezing with cryoprobe devices: [16,19,20,24]. [16,19] numerically investigated the temperature maps of a cold finger placed on a heart tissue on one side and with blood circulation on the other, while [20,24] investigated a similar geometry for ablation of cancer cells. Specifically [20] investigated how to

preserve healthy tissues in proximity to other diseased tissues that needs to be destroyed. This last point has to do with the aim of the present work, because the cells responsible for the arrhythmia must also be killed while the neighbouring cells of the phrenic nerve are preserved. In the present work, the cryoablation procedure is studied to achieve $-20 \div -25$ °C at the site where the cells responsible for the arrhythmia are located, i.e. at a distance of 0.25÷0.5 mm from the cryoprobe touching the inner wall of the pulmonary vein, while preserving the cells at a distance of more than 0.5 mm from the probe at temperatures higher than the entire range of damage ($-20 \div -25$ °C). This is the main task of the proposed activity, carried out through the development of an appropriate numerical model to describe the phenomenon of cryoablation.

2. Model

In order to model the behaviour of human tissue under severe cooling by a cryo-ablative device, it is necessary to calculate the heat propagation in the frozen and unfrozen regions, as well as the movement of the ice front and the exchange of latent heat associated with the phase change. In addition, there is a diffuse heat source due to local metabolism and heat removal (or supply) due to blood perfusion, i.e. circulation of the vascular system.

In the unfrozen region (V_u), heat transfer is governed by Pennes's bioheat eq. [25]:

$$c_u \frac{\partial T_u}{\partial t} = \vec{\nabla}\cdot(k_u \vec{\nabla} T_u) + \omega_b c_b (T_a - T_u) + \dot{q}_{met} \tag{1}$$

while in the frozen region (V_f) there is no blood perfusion ($\omega_{b,f} = 0$) and no metabolic heat generation ($\dot{q}_{met,f} = 0$), hence:

$$c_f \frac{\partial T_f}{\partial t} = \vec{\nabla}\cdot(k_f \vec{\nabla} T_f) \tag{2}$$

At the moving interface between the frozen and unfrozen phases (ice front), the temperature assumes the same value T_m, and the same heat fluxes. So, the following boundary conditions are set as:

$$T_u = T_f = T_m \tag{3}$$

$$k_f \frac{\partial T_f}{\partial \hat{n}} - k_u \frac{\partial T_u}{\partial \hat{n}} = q_l v_n \tag{4}$$

where $\partial T_f/\partial \hat{n}$ and $\partial T_u/\partial \hat{n}$ are the components of the temperature gradients perpendicular to the ice-front surface $\Gamma_m(\vec{r}, t) = 0$ direction, and close to the surface itself. Thus, the local normal to this surface is $\hat{n} = \vec{\nabla}\Gamma_m/|\vec{\nabla}\Gamma_m|$ (the m suffix stands for moist), that is:

$$\frac{\partial T_f}{\partial n} \equiv \vec{\nabla} T_f \cdot \frac{\vec{\nabla}\Gamma_m}{|\vec{\nabla}\Gamma_m|} \quad , \quad \frac{\partial T_u}{\partial n} \equiv \vec{\nabla} T_u \cdot \frac{\vec{\nabla}\Gamma_m}{|\vec{\nabla}\Gamma_m|} \tag{5}$$

while the term v_n is the normal velocity of the moving interface. Formally expressing it, if the vector position $\vec{r}$ at time t is on the interface Γ_m (i.e. $\Gamma_m(\vec{r}, t) = 0$), then the normal velocity to the surface is:

$$\vec{v}_n = \frac{\vec{r}_{dt} - \vec{r}}{dt} \tag{6}$$

where $\vec{r}_{dt}$ is defined by the following rule:

$$\Gamma_m\left(\vec{r}_{dt}, t + dt\right) = 0 \tag{7}$$

that is, given an ice front position at a defined time t, $\vec{r}_{dt}$ is the ice front position at the following time step $t + dt$. Thus, it satisfies the conditions:

$$\frac{\vec{r}_{dt} - \vec{r}}{\left|\vec{r}_{dt} - \vec{r}\right|} = \frac{\vec{\nabla}\Gamma_m}{|\vec{\nabla}\Gamma_m|} \tag{8}$$

The meaning of the symbols in eqs. (1) to (8)is shown in Table 1 [26] and Fig. 2:

Freezing of biological tissues occurs over a wide range of temperatures due to the inhomogeneity of the material. A range of −8 °C÷-1 °C is given in [27]. The authors cite [28,29] to set the upper limit between −0.5 °C and − 1 °C and the lower limit between −5 °C and − 8 °C. The width of this range is due to the differences between the freezing point of intracellular and extracellular fluids and cellular alterations due to multiple cycles of freezing and thawing. Cycles of freezing and thawing have been studied by Deng [26] for tumour ablation. The model here described follows this approach, i.e. the upper (top) and lower (bottom) limits of the freezing range are chosen as follows:

$$T_{m-up} = -1°C, \quad T_{m-low} = -8°C \tag{9}$$

In the effective (apparent) heat capacity method [11], the latent heat is approximated by a virtual heat capacity over the entire freezing temperature range $\left[T_{m-low}, \ T_{m-up}\right]$, which takes into account the latent heat absorbed during tissue freezing. The fraction of the two phases during freezing was evaluated by a smoothing function θ ranging from 1 (when the local temperature is equal to $T_{m\text{-}up}$) to 0 (when the local temperature is equal to $T_{m\text{-}low}$). The constitutive eqs. (1) to (4) can be resumed by:

$$c \frac{\partial T}{\partial t} = \nabla\cdot k \nabla T - \omega_b c_b (T_a - T) + \dot{q} \tag{10}$$

with c, k, $\dot{q}$, ω depending on the value of the local temperature T, according to Table 2:

The metabolic heat generation $\dot{q}_u$ and the blood perfusion rate ω_b are obviously not present in the frozen region.

3. The program

The explicit finite difference formulation is used to solve Eq. (10). The procedure is described in Appendix 1.

During freezing by the cryoballoon, a uniform heat power P, in the range from 4 to12 W, is absorbed from the inner surface of a sphere of radius $R = 14$ mm. The cooling inside the sphere is then transferred to the cryoballoon. This transfer is caused by the isenthalpic Joule-Thomson (or Joule-Kelvin) expansion of the nitrous oxide flowing through nozzles inside the balloon. The extracted heat flux per unit area

Table 1
List of symbols and values used.

symbol	Description	Units	value
c_b	blood vol. heat capacity	J·m^{-3}·K^{-1}	3.6·10^6
q_l	latent heat of freezing	J·m^{-3}	2.5·10^8
$\dot{q}_u$	metabolic heat generation per unit time	W·m^{-3}	4200
t	time	s	0 ÷ 100
r	distance	m	0 ÷ 0.03
T	temperature	°C	37 °C (at the beginning)
T_a	artery temperature	°C	37 °C
T_m	average freezing point	°C	−3.4 °C
ΔT	freezing range	°C	−8 ÷ −1 °C
ω_b	blood perfusion	s^{-1}	0.0005

symbol	Description	units	value	
			frozen	un-frozen
c	volumetric heat capacity	J·m^{-3}·K^{-1}	1.8·10^6	3.6·10^6
k	thermal conductivity	W·m^{-1}·K^{-1}	2	0.5

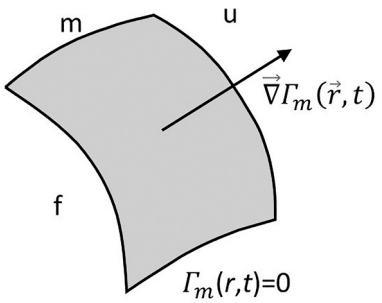

Fig. 2. meaning of symbols in Eq. (1–8): *f*: frozen region; *u*: unfrozen; *m*: mixing; $\Gamma_m(\vec{r},t)$: ice front surface; $\vec{\nabla}\Gamma_m(\vec{r},t)$: gradient of the ice front surface.

Table 2
Eq. (10) quantities.

–	*T* range		
	$T < T_{mlow}$	$T_{m-low} < T < T_{m-up}$	$T_{m-up} < T$
c	c_f	$\frac{q_l}{T_{m-up} - T_{m-low}} + (1-\theta)\cdot c_f + \theta\cdot c_u$	c_u
k	k_f	$(1-\theta)\cdot k_f + \theta\cdot k_u$	k_u
$\dot{q}$	0	0	$\dot{q}_u$
ω	0	0	ω_b

absorbed by the device is:

$$\varphi_q = \frac{P}{4\pi R^2} \tag{11}$$

The geometry of the cryoballoon (e.g. the next generation Arctic Front Advance [30], Fig. 1) is simulated with a sphere of 28 mm diameter (the effective diameter of the cryogenic device). The spatial interval of the *FD* model is set to 0.5 mm to obtain a good spatial resolution of the thermal field. Consequently, the time steps Δt are set to 0.005 s to meet the convergence and stability criteria.

The maximum values of the coordinates are set at $x_{\max}, y_{\max}, z_{\max} = 30\text{mm}$. With these limit values we assume negligible heat transfer and consequently negligible temperature variation, i.e. adiabatic conditions in this location. The initial temperature is that of the human body interior, i.e. 37 °C. Boundary conditions are: constant temperature at *x, y,* and *z* equal to 30 mm because at this distance and for the considered times the effect of freezing is negligible. On the cryo-balloon ($r = 14$ mm) the constant heat flux is imposed due to heat absorption at the sphere interior.

The quasi-spherical shape of the Medtronic cryoprobe (Fig. 1) with a diameter of 28 mm is well described by a spherical grid with the declared resolution (Fig. 3a). The symmetry of the sphere allows to model only one octal of the entire sphere (Fig. 3b).

4. Results

Fig. 4 shows the temperature trends at distances of 0 mm and 0.125 mm from the cryo-surface as a function of time for different heat powers *P* absorbed by the probe. Similar trends are obtained at other distances from the probe surface. The results show that the heat power has a strong influence on the cooling time. For $P > 6W$, the cooling trends converge more and more before freezing, but differ when the phase change is completed ($T = -8°C$). Fig. 4 clearly shows that the starting point of freezing approaches zero as the absorbed power increases.

Fig. 5 shows the temperature profiles as a function of time at different distances from the cryo-probe at a heating power of 12 W. Similar profiles are obtained for other values of the heating power *P*. These temperature trends are useful to evaluate the movement of the ice front: the intersection between these curves and the isotherm at $T_{m-low} = -8°C$ determines the time when the ice front reaches a distance *d*. Fig. 6 shows the spread of the ice front for different heating powers *P*.

Another important result of the model is the identification of the moving layer whose temperature is between −20 °C and − 25 °C, i.e. the layer where the permanent damage caused by freezing begins and is completed. This is possible looking at the intersection between the curves in Fig. 5 and the two isotherms at $T = -20°C$ and $T = -25°C$. These intersections are shown in Fig. 7 as a function of time for two absorbed powers (10 and 12 W). For example, Fig. 7 shows that at an absorbed power of 10 W, cells between 0.25 and 0.5 mm from the surface of the cryoprobe are frozen after about 55 s, the typical duration of cryotherapy, while cells above 0.5 mm are not frozen. At an absorbed power of 12 W, the same status is verified after 40 s. The two regions at the two powers are marked to better illustrate the difference: as the power increases, the slope of the region (and thus the treatment speed) also increases. In addition, the thickness of the band decreases and consequently the treated tissue portion becomes thinner. So as the power increases, the thickness of the damaged tissue is lower, but this procedure requires both a higher skill of the surgeon and more sophisticated instruments.

If the temperature of the cryoprobe is measured with a thermo-

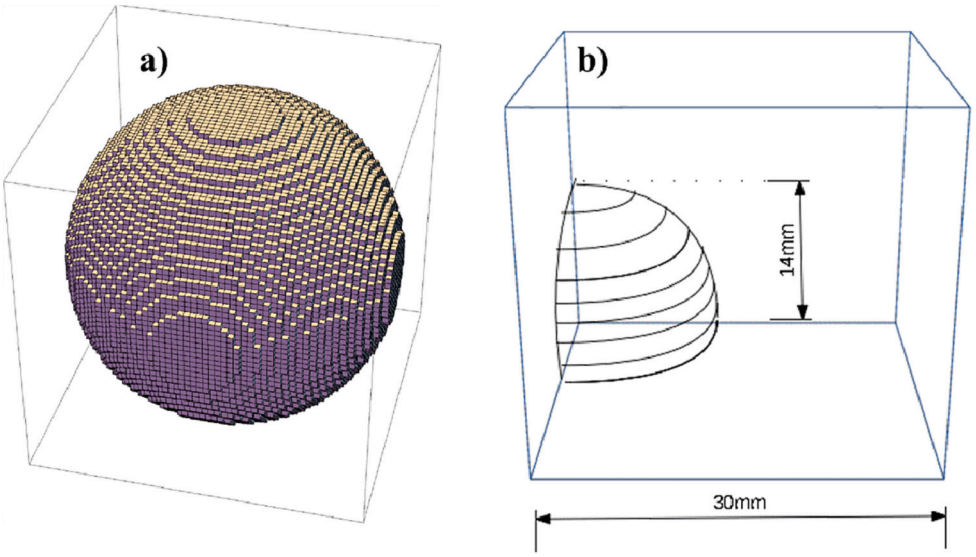

Fig. 3. a) Discretisation of the spherical cryoprobe; b) the octant top-front-right, i.e. with positive values for the coordinates x, y, z.

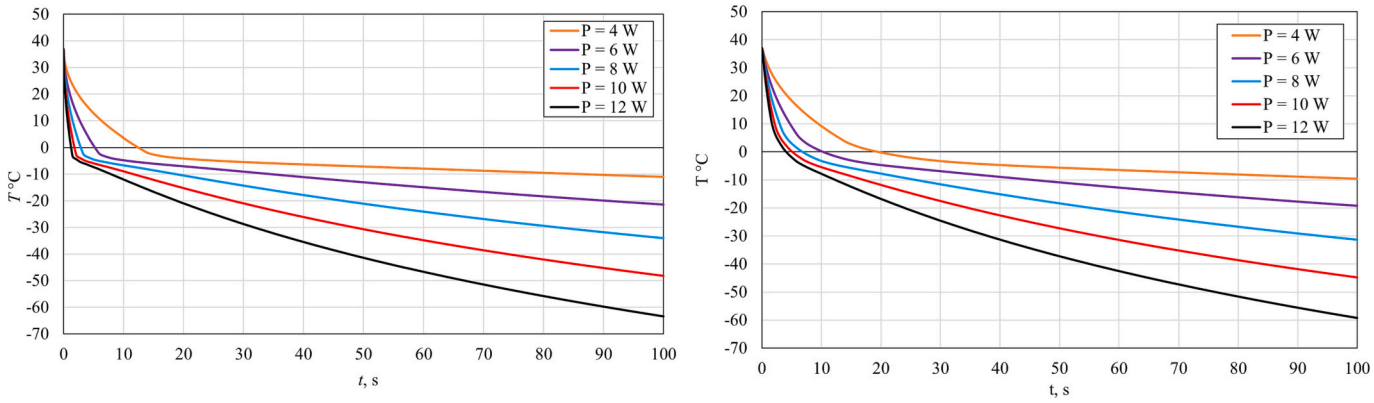

Fig. 4. Temperature profiles vs time at distance $d = 0$ mm (left) and $d = 0.125$ mm (right) from the probe surface.

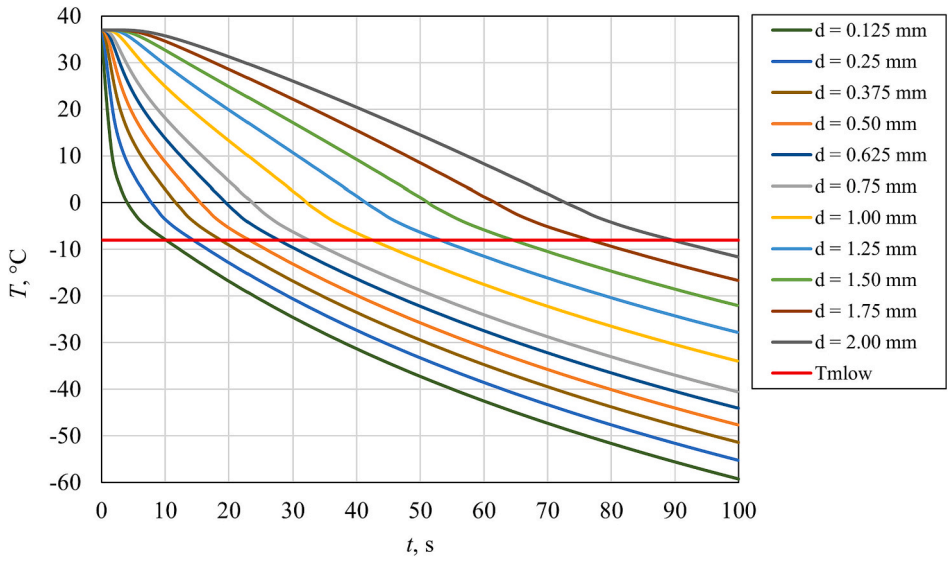

Fig. 5. Temperature evolution at different distances from the surface of the cryo-probe for 12 W absorbed power.

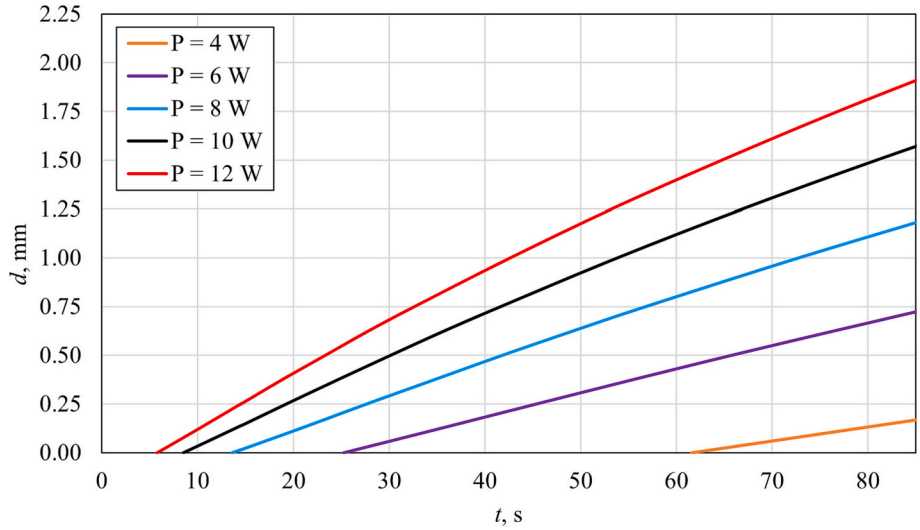

Fig. 6. Ice front propagation for different heat powers P.

couple, its output can be used to check the effectiveness of the treatment. In fact, there is a strong correlation between this temperature and the size of the frozen layer. Indeed, at $P = 10$ W, the temperature of the cryoprobe surface reaches −33 °C after 55 s (this time is required for the damage to reach the desired distance between 0.25 and 0.5 mm), while at $P = 12\,W$, this temperature is −35 °C after 40s, as shown in Fig. 4, left.

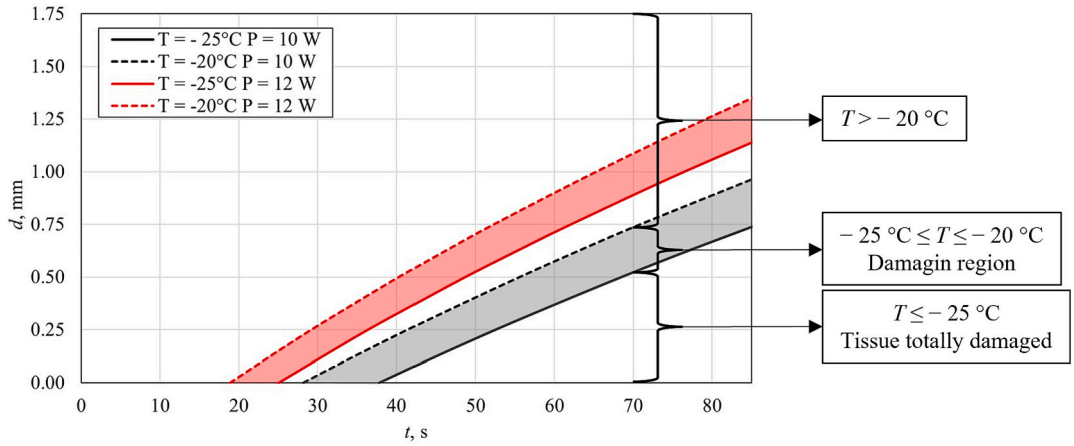

Fig. 7. Damaging region diagram: *d* is the distance from the cryo-balloon in the tissue.

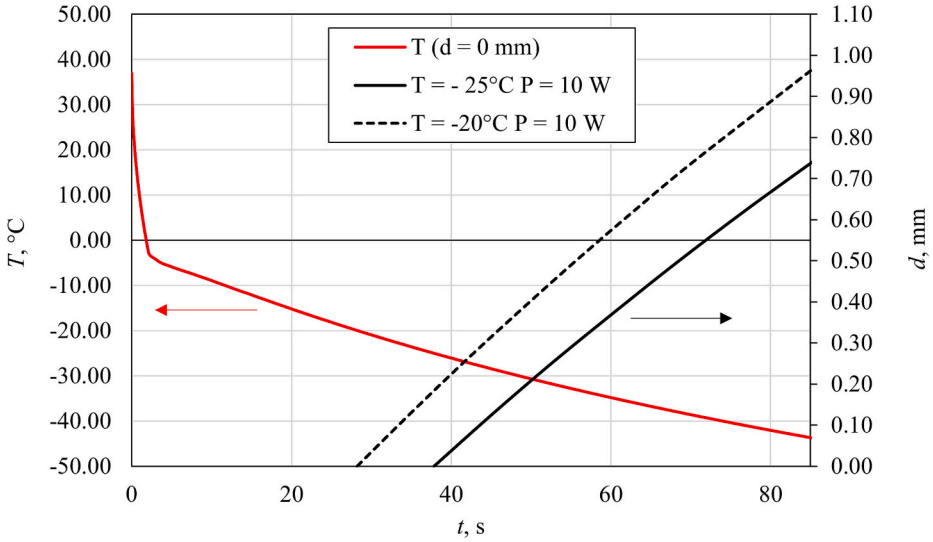

Fig. 8. Times to complete freezing in the objective layer for 10 W absorbed power.

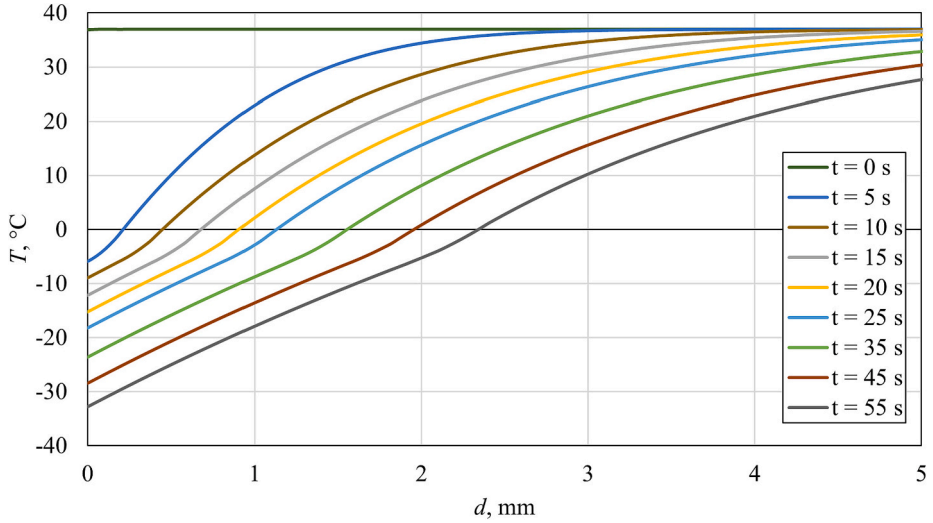

Fig. 9. Temperature profiles vs distance to probe *d* for different times.

Fig. 8 shows the same trends as Fig. 7, with the surface temperature of the cryoprobe superimposed. The correlation between the cryoprobe surface temperature and the cryoprobe application time could be extremely useful to the surgeon in determining the correct way to apply the therapy, as this temperature is detected by a thermocouple near the probe surface.

Fig. 5 also shows that, if −40 °C are reached at 0.375 mm from the cryo-probe surface (average distance of the zone to be ablated), temperature at distances higher than 0.5 mm result lower than −35 °C; that is zones that must be preserved are all the same damaged.

Fig. 9 shows temperature profiles as a function of the distance to the probe d for different times and 12 W absorbed power. This diagram can be used to estimate the most suitable times for performing the cryosurgical ablation. The curves show a flexus due to the phase change and the relative latent heat.

Fig. 10 shows the isothermal surfaces at $t = 55s$ and $P = 10\,W$ to point out the shape of these surfaces. Obviously, these surfaces result concentric spheres.

5. Clinical application

Cryoablation must ensure that the entire volume of the nerve tissue responsible for the arrhythmia is frozen in the shortest possible time and that in the meantime the other surrounding tissues are not damaged. In clinical practise, it has proved useful to keep the cryoprobe at −50 °C for 40÷60 s, depending on the results to be obtained. Under these conditions, Fig. 7 shows that at a power of 10 W, the tissue at a distance of 0.5 mm is ablated, while the other tissues more than 0.5 mm far from the probe surface remain at a temperature above −20 °C, i.e. undamaged. Of course, other combinations of powers and times are possible, so these results demonstrate the validity of the system used to evaluate the performance of the cryoprobes and to study possible variations of the procedure to optimise the therapeutic effect and reduce the risks. In this way, the clinical procedure can be adapted to patients with different ulcers and focal dimensions by changing the devices and procedure parameters to increase the effectiveness of the therapy.

6. Conclusions

Finite difference modelling of freezing by the cryogenic probe within the living cardiac tissue was performed to evaluate the propagation of the ice front and to determine the optimal clinical conditions for maximising the efficacy therapy during the internal cryoablation procedure. Although the modelled geometry is very simple, the approach can be easily extended to much more complicated probe geometries, as in the case of external cryoablation performed during open heart surgery by clamping the vein with a completely different device (e.g. the Surgical Ablation Probe [31]). The approach proved to be straightforward, functional to experimental needs and open to the study of more complex geometries and boundary conditions. If the assumed boundary conditions, test parameters (e.g. material properties, freezing temperatures and ranges) and tissue structure are more precisely defined, the model can still supply the expected results. Results are proved to be useful to establish the optimum choice of therapy parameters. As an example Fig. 4,Fig. 7 andFig. 8 show that an optimal combination of absorbed power and times guarantees the desired necrosis of the arrhythmia responsible tissues in due times (55 s). Experiments on biological tissue with similar geometries (pig heart) are in preparation to define the best settings to optimise the model. A future development of the model will also be the sensitivity analysis to find out which are the most important parameters influencing the results and to what extent.

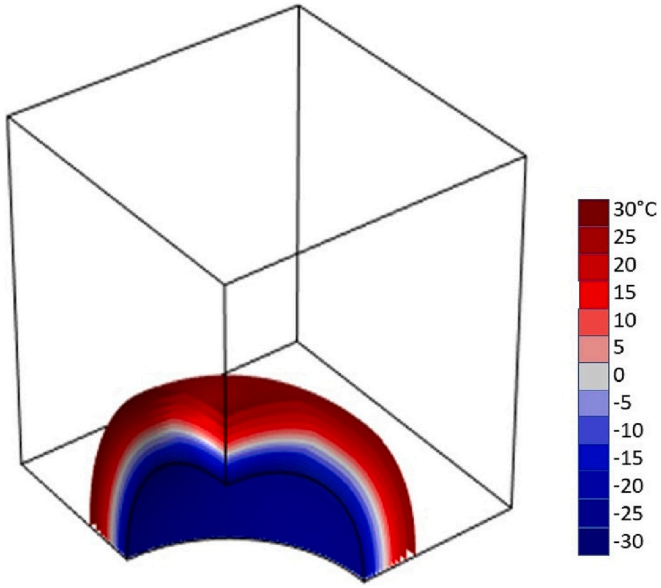

Fig. 10. Isothermal spherical surfaces at time $t = 55$ s with an absorbed power of 10 W.

CRediT authorship contribution statement

M. Potenza: Methodology, Software, Validation, Formal analysis, Data curation, Writing – original draft, Writing – review & editing. **C. Pisano:** Conceptualization, Methodology, Supervision. **P. Coppa:** Conceptualization, Software, Validation, Formal analysis, Writing – original draft, Writing – review & editing, Supervision. **G. Bovesecchi:** Validation, Formal analysis, Investigation, Writing – original draft, Writing – review & editing, Visualization. **S. Corasaniti:** Validation, Formal analysis, Investigation, Writing – original draft, Writing – review & editing, Supervision. **F. Barbero:** Software, Formal analysis, Investigation, Data curation, Writing – original draft.

Declaration of Competing Interest

The authors declare that they have no known competing financial interests or personal relationships that could have appeared to influence the work reported in this paper.

Data availability

Data will be made available on request.

Appendix 1. Development of the finite difference Pennes's heat transfer propagation eq. [25]

The general position in the tested volume ($r = xe_x + ye_y + ze_z$) is replaced by a grid of points:

$$r_{j,k,m} = x_j e_x + y_k e_y + z_m e_z \tag{12}$$

with the space and time steps given by:

$$\Delta r = \frac{x_j}{j-1} = \frac{y_k}{k-1} = \frac{z_m}{m-1} \quad \text{and} \quad \Delta t = \frac{t_i}{i-1} \tag{13}$$

respectively.

Because of the central symmetry, the integration volume can be limited to one octant of the sphere (Fig. 3b and Fig. 10), corresponding to positive values of the coordinates x, y, z. Boundary conditions are insulated surfaces at $x = 0$, $y = 0$ and $z = 0$, for symmetry.

Temperatures T are functions of time t_i and of the spatial coordinates x_j, y_k, z_m. Their values are represented by a matrix $T_{i,j,k,m}$, with initial

conditions $T_{1,j,k,m}$ at uniform temperature (37 °C). To make the development of the algorithm easier, a matrix $M_{j,k,m}$ is associated to the matrix $T_{i,j,k,m}$, with the following definition of indexes:

$$M_{j,k,m} = \begin{cases} -1 & \text{for} \quad r_{j,k,m} < R - dr\sqrt{3} \\ 0 & \text{for} \quad (j_{\max} - j)(k_{\max} - k)(m_{\max} - m) = 0 \\ 1 & \text{for} \quad r_{j,k,m} > R \text{ and } (j_{\max} - j)(k_{\max} - k)(m_{\max} - m) \neq 0 \\ 2 & \text{for} \quad R - dr\sqrt{3} \leq r_{j,k,m} \leq R \end{cases} \tag{14}$$

with:

$$r_{j,k,m} = \sqrt{\left(x_j^2 + y_k^2 + z_m^2\right)} \tag{15}$$

At points $r_{j,k,m}$ with $M_{j,k,m} = 1$ the solution of the bio-heat eq. (10) is obtained calculating

$$\begin{aligned} T_{i+1,j,k,m} = &\left\{[1 - w(1-\beta) - 6Fo]T_{i,j,k,m} + \right. \\ &+Fo\left[T_{i,j+1,k,m} + T_{i,j-1,k,m} + T_{i,j,k+1,m} + T_{i,j,k-1,m} + T_{i,j,k,m+1} + T_{i,j,k,m-1}\right] + \\ &\left.+(q + \omega_b c_b T_a)\Delta t\right\}/(1 + w\beta) \end{aligned} \tag{16}$$

With:

$$w = \frac{\omega_b c_b}{c}\Delta t \quad \text{and} \quad \mathrm{Fo} = \frac{k\Delta t}{c\ \Delta r^2} \tag{17}$$

With Fo the Fourier dimensionless number. Material properties are evaluated at intermediate values between times t_i and $t_i + \Delta t$. The term $\beta \in [0, 1]$, called relaxation factor, defines temperatures $T^*_{i,j,k,m}$ at an intermediate time, and is given by:

$$T^*_{i,j,k,m} = \beta T_{i+1,j,k,m} + (1 - \beta)T_{i,j,k,m}, \tag{18}$$

By replacing the expression (18) in the discretized form of eq. (10), eq. (16) is obtained. If $\beta = 0.5$ is chosen, as in the present case, it corresponds exactly to halfway between t_i and$t_i + \Delta t$.

Before calculating the eq. (16) in points having $M = 1$, we must scan all the other sectors associated to the boundary conditions. For $M_{j,k,m} = -1$ we are beyond the domain of interest (it is inside the balloon) and the algorithm keeps an artificial value, of no interest whatsoever. For $M_{j,k,m} = 0$ we are at the outer boundary and we set $T_{i,j,k,m} = 37°C$. At points $r_{1,k,m}, r_{j,1,m}, \ r_{j,k,1}$ we are at the lateral planes $x = 0, y = 0, z = 0$, respectively, and we set no transversal heat flux, that is to say:

$$T_{i,1,k,m} = T_{i,2,k,m} \tag{19}$$

$$T_{i,j,1,m} = T_{i,j,2,m} \tag{20}$$

$$T_{i,j,k,1} = T_{i,j,k,2} \tag{21}$$

For each point $r_{i,j,k}$ having $M_{i,j,k} = 1$, we also must assign artificial temperatures to the surrounding points if they belong to the inner layer marked by $M = 2$. Those temperatures are calculated according to the boundary condition of a heat flux φ, whose vector form is:

$$\varphi = \varphi^{(x)}e_x + \varphi^{(y)}e_y + \varphi^{(z)}e_z, \qquad \text{with} \quad \begin{cases} \varphi^{(x)} = -\varphi_q x/r \\ \varphi^{(y)} = -\varphi_q y/r \\ \varphi^{(z)} = -\varphi_q z/r \end{cases} \tag{22}$$

r given by eq. (15). Being $\varphi^{(x)} = -kdT/dr$ the first heat flux component and having set $\Delta x = \Delta r$, we have:

$$\varphi^{(x)}_{j\pm1,k,m} = \begin{cases} \\ = -\varphi_q \dfrac{x_{j\pm1}}{r_{j\pm1,k,m}} \\ \\ = \mp k\left(T_{i,j,k,m}\right)\dfrac{T_{i,j\pm1,k,m} - T_{i,j,k,m}}{\Delta r} \end{cases} \qquad for \quad M_{j\pm1,k,m} = 2 \tag{23}$$

whence:

$$T_{i,j\pm1,k,m} = \pm\frac{\varphi x_{j\pm1}\Delta r}{k\left(T_{i,j,k,m}\right)r_{j\pm1,k,m}} + T_{i,j,k,m} \quad \text{if} \quad M_{j\pm1,k,m} = 2 \tag{24}$$

Similarly, from the heat flux components $\varphi^{(y)}$ and $\varphi^{(z)}$ it is:

$$T_{i,j,k\pm1,m} = \pm\frac{\varphi y_{k\pm1}\Delta r}{k\left(T_{i,j,k,m}\right)r_{j,k\pm1,m}} + T_{i,j,k,m} \quad \text{if} \quad M_{j,k\pm1,m} = 2 \tag{25}$$

$$T_{i,j\pm1,k,m} = \pm\frac{\varphi z_{m\pm1}\Delta r}{k\left(T_{i,j,k,m}\right)r_{j,k,m\pm1}} + T_{i,j,k,m} \quad \text{if} \quad M_{j,k,m\pm1} = 2 \tag{26}$$

For each point $r_{i,j,k}$ we must insert the synthetic temperatures given by eqs. (21) to (26) in eq. (16). This grants a correct representation of the heat flux at the border of the cryo-device.

References

[1] H. Calkins, G. Hindricks, R. Cappato, et al., 2017/HRS/EHRA/ECAS/APHRS/SOLAECE expert consensus statement on catheter and surgical ablation of atrial fibrillation, Heart Rhythm. 14 (10) (2017) 275–444, https://doi.org/10.1016/j.hrthm.2017.05.012.

[2] K.-H. Kuck, J. Brugada, A. Fürnkranz, et al., Cryoballoon or radiofrequency ablation for paroxysmal atrial fibrillation, N. Engl. J. Med. 374 (23) (2016) 2235–2245, https://doi.org/10.1056/NEJMoa1602014.

[3] https://youtu.be/ZSlnI6YN7p4.

[4] Barbero, F., Bovesecchi, G., Coppa P. et al., V. "Testing the physical core of cryoballoon probe: the medical needs behind a complex thermofluid behavior". Proc. of the XVIII AIPT Meeting, 22nd of September 2018, 125–134, Padua, Italy.

[5] W. Su, R. Kowal, M. Kowalski, et al., Best practice guide for cryoballoon ablation in atrial fibrillation: the compilation experience of more than 3000 procedures, Heart Rhythm. 12 (7) (2015) 1658–1666, https://doi.org/10.1016/j.hrthm.2015.03.021.

[6] J. Andrade, P. Khairy, M. Dubuc, Catheter cryoablation: biology and clinical uses, Circ. Arrhythm. Electrophysiol. 6 (1) (2013) 218–227, https://doi.org/10.1161/CIRCEP.112.973651.

[7] K.M. Gürses, M.U. Yalçin, Koçyigit, et al., OP-285 what lies beneath the cryoballoon ablation with the new arctic front advance cryoballoon: higher incidence of phrenic nerve palsy, Am. J. Cardiol. 113 (7) (2014) S68, https://doi.org/10.1016/j.amjcard.2014.01.189.

[8] T.J. Bunch, G.K. Bruce, S. Mahapatra, et al., Mechanisms of phrenic nerve injury during radiofrequency ablation at the pulmonary vein orifice, J. Cardiovasc. Electrophysiol. 16 (12) (2005) 1318–1325, https://doi.org/10.1111/j.1540-8167.2005.00216.x.

[9] V. Giaretto, C. Passerone, Mirror image technique for the thermal analysis in cryoablation: experimental setup and validation, Cryobiology 79 (2017) 56–64, https://doi.org/10.1016/j.cryobiol.2017.09.001.

[10] Z. Wang, G. Zhao, T. Wang, et al., Three-dimensional numerical simulation of the effects of fractal vascular trees on tissue temperature and intracellular ice formation during combined cancer therapy of cryosurgery and hyperthermia, Appl. Therm. Eng. 90 (2015) 296–304, https://doi.org/10.1016/j.applthermaleng.2015.06.103.

[11] Y. Zhang, K. Du, J. He, et al., Impact factors analysis of the enthalpy method and the effective heat capacity method on the transient nonlinear heat transfer in phase change materials (PCMs), Num. Heat Transf. Part A: Appl. 65 (1) (2014) 66–83, https://doi.org/10.1080/10407782.2013.811153.

[12] M.K. Getman, E. Wissner, R. Ranjan, J.P. Lalonde, Relationship between time-to-isolation and freeze duration: computational modeling of dosing for Arctic front advance and Arctic front advance pro cryoballoons, J. Cardiovasc. Electrophysiol. 30 (11) (2019) 2274–2282, https://doi.org/10.1111/jce.14150.

[13] N. Coulombe, J. Paulin, W. Su, Improved in vivo performance of second-generation cryoballoon for pulmonary vein isolation, J. Cardiovasc. Electrophysiol. 24 (8) (2013) 919–925, https://doi.org/10.1111/jce.12157.

[14] https://www.bostonscientific.com/en-EU/medical-specialties/electrophysiology/arrhythmias/single-shot-ablation.html.

[15] J. Mojica, F. Lipartiti, M. Al Housari, et al., Procedural safety and efficacy for pulmonary vein isolation with the novel PolarxTM cryoablation system: a propensity score matched comparison with the Arctic frontTM cryoballoon in the setting of paroxysmal atrial fibrillation, J. Atrial. Fibrillat. 14 (1), 20200455 (2021), https://doi.org/10.4022/jafib.20200455.

[16] M. Handler, G. Fischer, M. Seger, et al., Simulation and evaluation of freeze-thaw cryoablation scenarios for the treatment of cardiac arrhythmias, Biomed. Eng. Online 14 (2015) 12, https://doi.org/10.1186/s12938-015-0005-9.

[17] T. Weimar, A.M. Lee, S. Ray, et al., Evaluation of a novel cryoablation system: in-vitro testing of heat capacity and freezing temperatures, Innovations (Phila) 7 (6) (2012) 403–409, https://doi.org/10.1177/155698451200700606.

[18] A.A. Gage, J.M. Baust, J.G. Baust, Experimental cryosurgery investigations in vivo, Cryobiology 59 (3) (2009) 229–243, https://doi.org/10.1016/j.cryobiol.2009.10.001.

[19] M. Handler, G. Fischer, M. Seger, et al., Computer simulation of cardiac cryoablation: comparison with in vivo data, Med. Eng. Phys. 35 (12) (2013) 1754–1761, https://doi.org/10.1016/j.medengphy.2013.07.006.

[20] K.J. Chua, S.K. Chou, On the study of the freeze–thaw thermal process of a biological system, Appl. Therm. Eng. 29 (17–18) (2009) 3696–3709, https://doi.org/10.1016/j.applthermaleng.2009.07.001.

[21] H.F. Tse, K.L. Ripley, K.L.F. Lee, et al., Effects of temporal application parameters on lesion dimensions during transvenous catheter cryoablation, J. Cardiovasc. Electrophysiol. 16 (2) (2005) 201–204, https://doi.org/10.1046/j.1540-8167.2005.40559.x.

[22] J. Martí-Almor, M.E. Jauregui-Abularach, B. Benito, et al., Pulmonary hemorrhage after cryoballoon ablation for pulmonary vein isolation in the treatment of atrial fibrillation, Chest. 145 (1) (2014) 156–157, https://doi.org/10.1378/chest.13-0761.

[23] W. Su, A. Aryana, R. Passman, et al., Cryoballoon best practices II: practical guide to procedural monitoring and dosing during atrial fibrillation ablation from the perspective of experienced users, Heart Rhythm. 15 (9) (2018) 1348–1355, https://doi.org/10.1016/j.hrthm.2018.04.021.

[24] K.J. Chua, S.K. Chou, J.C. Ho, An analytical study on the thermal effects of cryosurgery on selective cell destruction, J. Biomech. 40 (1) (2007) 100–116, https://doi.org/10.1016/j.jbiomech.2005.11.005.

[25] H. Pennes, Analysis of tissue and arterial blood temperatures in the resting human forearm, J. Appl. Physiol. 1 (2) (1948) 93–122, https://doi.org/10.1152/jappl.1948.1.2.93.

[26] Z. Deng, J. Liu, Numerical simulation of 3-D freezing and heating problems for combined cryosurgery and hyperthermia therapy, Num. Heat Transf. Part A: Appl. 46 (6) (2004) 587–611, https://doi.org/10.1080/10407780490487740.

[27] Y. Rabin, A. Shitzer, Numerical solution of the multidimensional freezing problem during cryosurgery, J. Biomech. Eng. 120 (1) (1998) 32–37, https://doi.org/10.1115/1.2834304.

[28] P. Altman, D.S. Dittmer, Respiration and Circulation, Federation of American Societies for Experimental Biology, Bethesda MD, 1971.

[29] F. Wessling, P. Blackshear, The thermal properties of human blood during the freezing process, J. Heat Transf. 95 (2) (1973) 246–249, https://doi.org/10.1115/1.3450035.

[30] A. Fürnkranz, S. Bordignon, B. Schmidt, Et al. "Improved procedural efficacy of pulmonary vein isolation using the novel second-generation cryoballoon, J. Cardiovasc. Electrophysiol. 24 (5) 492–497, doi:10.1111/jce.12082.

[31] B. Johansson, B. Houltz, N. Edvardsson, et al., Cardiac function in relation to rhythm outcome after intraoperative epicardial left atrial cryoablation, Scand. Cardiovasc. J. 45 (6) (2011) 327–335, https://doi.org/10.3109/14017431.2011.592855.